



Crystal structure and low-energy Einstein mode in $\text{ErV}_2\text{Al}_{20}$ intermetallic cage compound



Michał J. Winiarski*, Tomasz Klimczuk

Faculty of Applied Physics and Mathematics, Gdansk University of Technology, Narutowicza 11/12, 80-233 Gdansk, Poland

ARTICLE INFO

Keywords:

Intermetallic compounds
 $\text{CeCr}_2\text{Al}_{20}$ -type structure
 Magnetic properties
 Specific heat measurements

ABSTRACT

Single crystals of a new ternary aluminide $\text{ErV}_2\text{Al}_{20}$ were grown using a self-flux method. The crystal structure was determined by powder X-ray diffraction measurements and Rietveld refinement, and physical properties were studied by means of electrical resistivity, magnetic susceptibility and specific heat measurements. These measurements reveal that $\text{ErV}_2\text{Al}_{20}$ is a Curie-Weiss paramagnet down to 1.95 K with an effective magnetic moment $\mu_{\text{eff}} = 9.27(1) \mu_B$ and Curie-Weiss temperature $\Theta_{\text{CW}} = -0.55(4)$ K. The heat capacity measurements show a broad anomaly at low temperatures that is attributed to the presence of a low-energy Einstein mode with characteristic temperature $\Theta_E = 44$ K, approximately twice as high as in the isostructural ‘Einstein solid’ $\text{VAl}_{10.1}$.

1. Introduction

Ternary aluminides $RT_2\text{Al}_{20}$ (R =electropositive elements, T =early 3d, 4d, and 5d transition metals) crystallizing in the $\text{CeCr}_2\text{Al}_{20}$ -type structure have recently attracted much scientific interest, due to their versatility towards the chemical composition and a variety of interesting physical properties, depending on the constituent elements.

The unit cell of a $\text{CeCr}_2\text{Al}_{20}$ -type compound is shown in Fig. 1. A characteristic feature of this structure is the presence of large ‘cages’ formed by Al atoms surrounding the electropositive R atom (occupying the Wyckoff position 8a). Such cages of various shapes and sizes are also found eg. in dodecaboride ZrB_{12} [1], clathrates including $\text{Ba}_8\text{Si}_{46}$, $\text{Ba}_{24}\text{Si}_{100}$ [2], $\text{Ba}_8\text{Au}_{16}\text{P}_{30}$ [3], $\text{Na}_{24}\text{Si}_{136}$ [4], filled skutterudites [5–7] and in the β -pyrochlore oxides AOs_2O_6 (A =alkaline metals) [8] (see Fig. 2). In these systems low-energy, large amplitude, localized (related to a specific crystallographic site) anharmonic vibrations of small cage-filling atoms are observed. This ‘rattling’ of cage filling atoms affects thermal and transport properties of materials, resulting eg. in suppression of the lattice thermal conductivity [3,5,9] that can lead to an increase in the thermoelectric figure of merit (ZT) [3,5]. The presence of ‘rattling’ phonons is also found to enhance the superconducting critical temperature in hexa- and dodecaborides [1,10,11], β -pyrochlores [8,12], and $\text{CeCr}_2\text{Al}_{20}$ -type compounds: $\text{Al}_x\text{V}_2\text{Al}_{20}$ [13–15], $\text{Ga}_x\text{V}_2\text{Al}_{20}$ [14,16], and $\text{RV}_2\text{Al}_{20}$ (R =Sc, Y, Lu) [17]. The contribution of ‘rattling’ phonons to the specific heat are usually well described using the Einstein model with a low characteristic (Einstein) temperature Θ_E .

The introduction of 4f elements into the 8a position of a $\text{CeCr}_2\text{Al}_{20}$ structure leads to a variety of magnetic properties. $\text{LaV}_2\text{Al}_{20}$ was found

to exhibit strong diamagnetism [27] resulting from a peculiar Fermi surface [28]. $\text{CeT}_2\text{Al}_{20}$ (T =Ti, V, Cr) are found to exhibit Pauli paramagnetism, consistent with a nonmagnetic tetravalent configuration of the Ce atom [29,30]. $\text{PrT}_2\text{Al}_{20}$ (T =Ti, V) are exotic superconductors in which the superconducting state coexists with the quadrupolar order [31–34], while $\text{PrCr}_2\text{Al}_{20}$ was described as a paramagnetic Kondo lattice [30]. $\text{NdTi}_2\text{Al}_{20}$ is an antiferromagnet (AFM) with the Néel temperature $T_N=1.45$ K [35], $\text{NdV}_2\text{Al}_{20}$ and $\text{NdCr}_2\text{Al}_{20}$ in turn are ferromagnets (FM) with the Curie temperature $T_C=1.8$ K and 1.7 K, respectively [35]. In $\text{SmT}_2\text{Al}_{20}$ (T =Ti, V, and Cr) AFM transition ($T_N=6.4$, 2.9 and 1.8 K, respectively) was observed along with strong valence fluctuations and a Kondo effect [36], similarly $\text{SmTa}_2\text{Al}_{20}$ shows strong electron correlation effects [37]. $\text{EuV}_2\text{Al}_{20}$ was found to exhibit a Kondo lattice behavior [38] and $\text{EuCr}_2\text{Al}_{20}$ shows an AFM transition ($T_N=4.8$ K) due to the magnetic moments carried on a divalent Eu ion [39]. $\text{GdTi}_2\text{Al}_{20}$, $\text{GdV}_2\text{Al}_{20}$, and $\text{GdCr}_2\text{Al}_{20}$ are reported AFMs with $T_N=2.6$, 2.4–3.1, and 3.9 K [40,41], respectively. $\text{TmTi}_2\text{Al}_{20}$ was recently found to exhibit an AFM transition at 0.7 K [42], while no magnetic ordering is observed in $\text{TmV}_2\text{Al}_{20}$ down to 0.5 K [43]. $\text{YbT}_2\text{Al}_{20}$ (T =Ti, V, Cr) are Pauli paramagnets with a divalent Yb ion [44] and $\text{LuV}_2\text{Al}_{20}$ was found to exhibit a SC transition with the critical temperature $T_c=0.6$ K [17]. Although some of the Tb, Dy, Ho, and Er-bearing compounds are reported [45], their physical properties remain unknown.

In this study we present single-crystal growth and physical characterization of a previously unreported $\text{ErV}_2\text{Al}_{20}$ intermetallic. The crystal structure of the new compound is described along with results of magnetic susceptibility, electrical resistivity and specific heat

* Corresponding author.

E-mail address: mwiniarski@mif.pg.gda.pl (M.J. Winiarski).

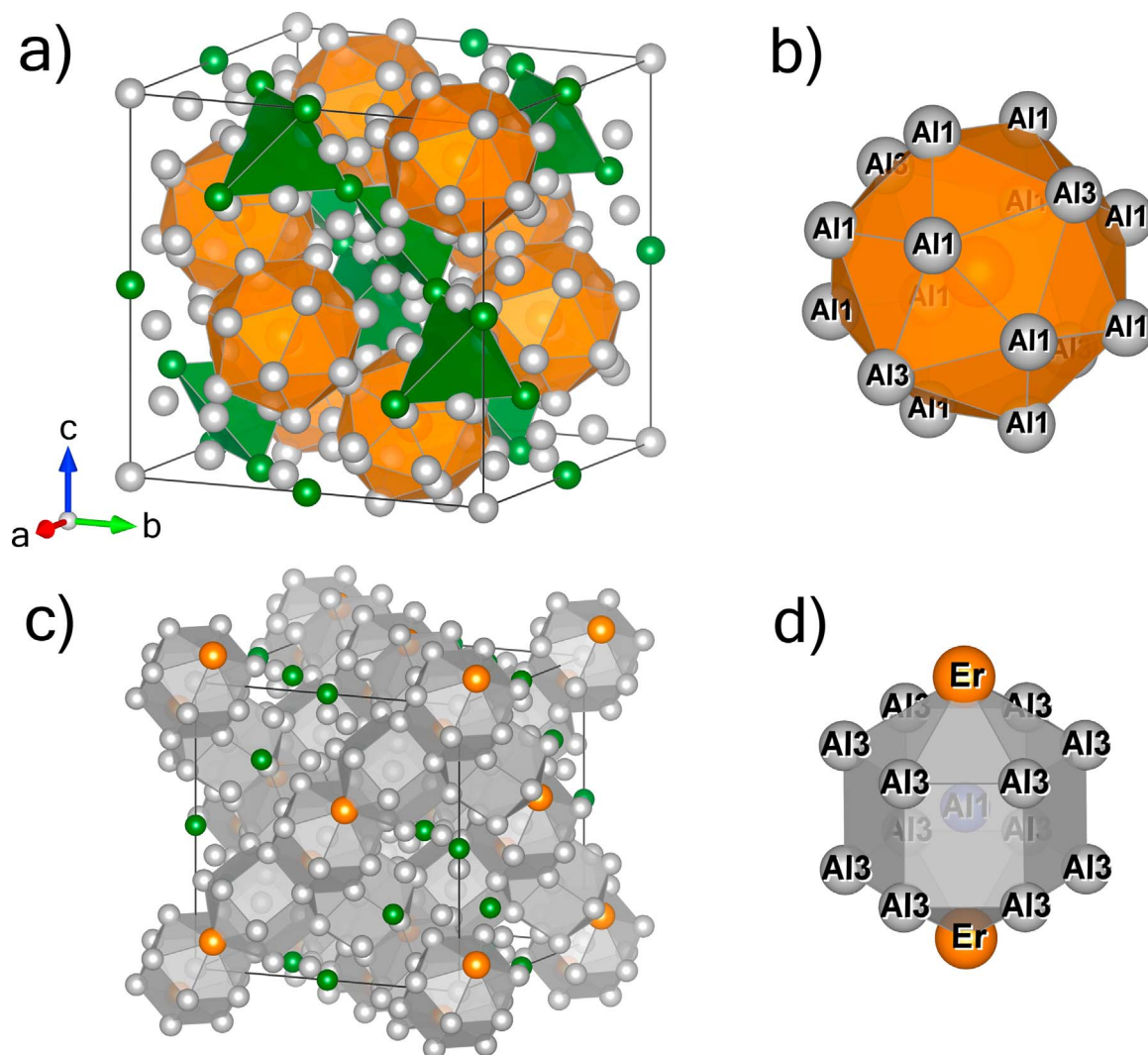


Fig. 1. Unit cell of $\text{ErV}_2\text{Al}_{20}$. (a) Er atoms (orange), arranged in a diamond lattice, are positioned inside Frank-Kasper CN 16 polyhedra [18] (Panel b) formed by Al1(16c) and Al3(96g) atoms (silver). V atoms (green) form a pyrochlore array [19]. (c,d) Al1(16c) atoms are engaged in Frank-Kasper CN 14 polyhedra formed by Al3(96g) and Er(8a). Image was rendered using VESTA software [20]. Fig. S1 of Supplementary material shows the relationships between the $\text{CeCr}_2\text{Al}_{20}$, ZrZn_{22} , and $\text{Mg}_3\text{Cr}_2\text{Al}_{18}$ -type structures. (For interpretation of the references to color in this figure legend, the reader is referred to the web version of this article.)

measurements.

2. Materials and methods

Single crystals of $\text{ErV}_2\text{Al}_{20}$ were grown using an Al self-flux method [46]. Erbium (99.9% purity), vanadium (99.8%), and aluminum (99.999%) pure metals were put together in an alumina crucible at the atomic ratio of 1:2:90 (Er:V:Al). A frit-disc and a second crucible were used for flux separation as it is described in ref. [47]. The crucible set was then sealed in an evacuated quartz tube backfilled with Ar to dilute the Al vapor attacking the tube walls.

The ampoule was then placed in a furnace, heated at $100\text{ }^\circ\text{C/h}$ to $1070\text{ }^\circ\text{C}$, held for 2 h, and then slowly cooled ($4\text{ }^\circ\text{C/h}$) to $770\text{ }^\circ\text{C}$ at which temperature it was centrifugated to separate crystals from the remaining flux. Crystals with sizes up to a few millimeters were obtained.

Crystals were then etched in ca. 0.1 M sodium hydroxide (NaOH) solution for a few hours to remove the Al flux droplets that remained after centrifugation.

Powder X-ray diffraction (XRD) patterns were collected on pulverized single-crystals using PANalytical X'Pert Pro diffractometer with Cu K_α source. To prevent the effect of preferred orientation along the [111] direction several small single crystals were first fine ground using an

agate mortar and pestle and the resulting powder was spilled onto a spot of Apiezon M grease on a sample holder. FullProf software package [48] was used for the Rietveld refinement [49] of the structure model derived from crystallographic data for $\text{GdV}_2\text{Al}_{20}$ [41].

Resistivity measurements were carried out by the four contact method in a Quantum Design Physical Properties Measurement System (PPMS) on a single crystal sample cut and polished into a rectangular plate. Electrical leads were made of $\text{Ø}0.04\text{ mm}$ platinum wires glued to the sample surface using a silver paste. Magnetic susceptibility measurements were done on etched single crystals using the ACMS option of PPMS in a temperature range of 1.95–300 K. Several randomly-oriented single crystals were taken and put in a standard straw sample holder. Specific heat measurements were carried out using the PPMS Heat Capacity option by means of the standard 2 τ relaxation method.

3. Results

3.1. Crystallographic structure

Fig. 3 presents the powder XRD pattern collected on pulverized single crystals of $\text{ErV}_2\text{Al}_{20}$ along with a Rietveld fit to the data. Analysis of the diffraction reflections showed that the sample contained approx.

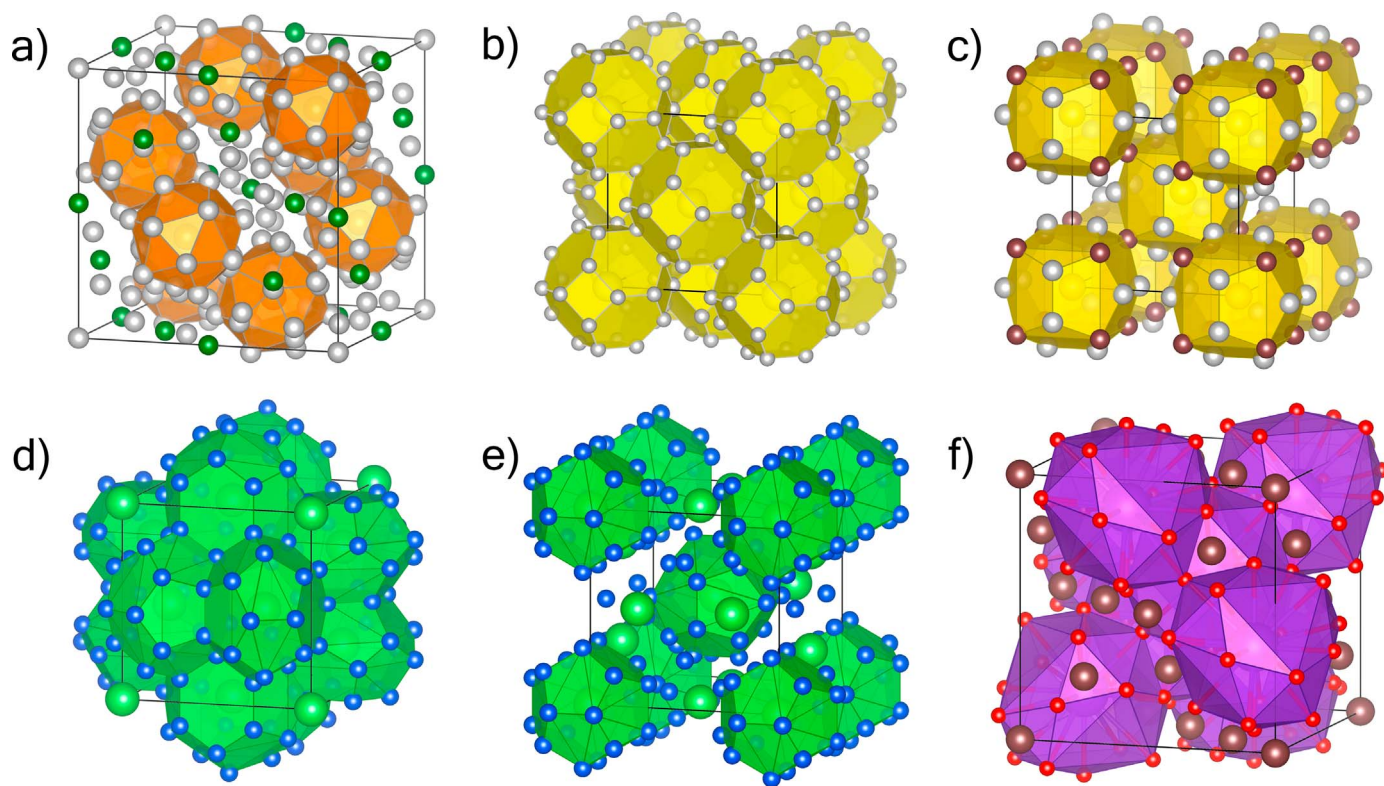


Fig. 2. Comparison of cage-type crystal structures: (a) CeCr₂Al₂₀-type ErV₂Al₂₀, (b) ZrB₁₂ dodecaboride (Zr atoms – yellow, B – silver) [21,22], (c) PrOs₄Sb₁₂ filled skutterudite (Pr – yellow, Os – brown, Sb – silver) [23,24], (d,e) Ba₈Si₄₆ clathrate (Ba – green, Si – blue) [22,25], with two distinct Ba-Si cage types, (f) KOs₂O₆ β-pyrochlore (K – purple, Os – brown, O – red) [22,26]. (For interpretation of the references to color in this figure legend, the reader is referred to the web version of this article.)

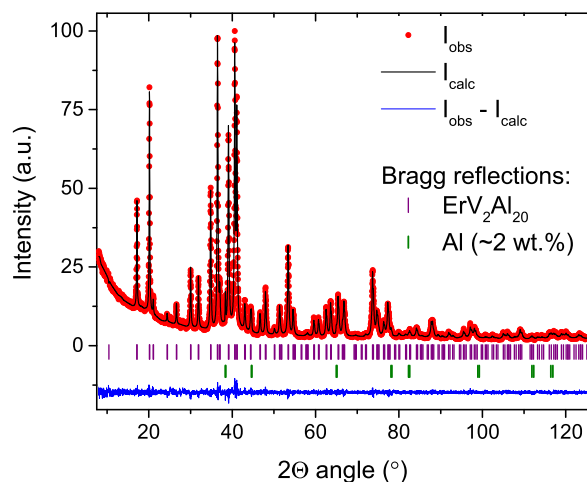


Fig. 3. Fit (black) to the experimental powder X-ray diffraction pattern of pulverized ErV₂Al₂₀ crystals (red points). The difference profile ($I_{\text{obs}} - I_{\text{calc}}$) is shown as a blue line. Purple and green ticks mark the positions of Bragg reflections for ErV₂Al₂₀ and Al impurity, respectively. The slightly higher background around $2\theta \approx 40^\circ$ comes from the Apiezon M grease used for sticking powder to the sample holder. (For interpretation of the references to color in this figure legend, the reader is referred to the web version of this article.)

2 wt% of Al that remained after etching in NaOH solution.

Table 1 presents the crystallographic structure parameters derived from the Rietveld fit. Lattice constant of ErV₂Al₂₀ $a=14.5175(2)$ Å was found to be slightly larger than reported for TmV₂Al₂₀ (14.5024 Å) [43] and LuV₂Al₂₀ (14.5130 Å) and smaller than for DyV₂Al₂₀ (14.54 Å) [45], in agreement with the lanthanide contraction effect (see Fig. 4). The unit cell parameter of ErV₂Al₂₀ was found to be larger than for ErCr₂Al₂₀ and smaller than for ErTi₂Al₂₀ (see inset of Fig. 4), in consistency with behavior of the whole CeCr₂Al₂₀-type family.

3.2. Electrical resistivity

Resistivity of ErV₂Al₂₀ shows metallic-like character as it is shown in Fig. 5(a). Since the single crystal used for measurements was cut and its surface was polished, the contribution of Al flux spots to the sample resistivity can be considered negligible. The low-temperature resistivity was found to show a complex character that cannot be fitted by simple models (see Fig. 5(b)). The unusual T-dependence of resistivity results from the presence of a low-energy Einstein phonon mode (see the *Specific heat* paragraph below). It was shown by Cooper [53] that the contribution of an Einstein mode to the resistivity can be described using an equation:

$$\rho_{\text{Einstein}}(T) = \frac{KN}{MT(\exp(\frac{\Theta_E^*}{T}) - 1)(1 - \exp(-\frac{\Theta_E^*}{T}))} \quad (1)$$

where M is the mass of the oscillator, N is the number of oscillators per unit volume, K is a parameter dependent on the electron density and the strength of the coupling between electrons and local mode phonons, and Θ_E^* is the characteristic temperature of the Einstein mode (Einstein temperature). While this equation was successfully used for fitting the resistivity data of ‘Einstein solids’ VAl_{10+x} and Ga_xV₂Al₂₀ [16,53], in the case of ErV₂Al₂₀ it was necessary to include additional terms, as is shown in Eq. (2):

$$\rho(T) = \rho_0 + \rho_{\text{Einstein}}(T) + AT^2 + BT^5 \quad (2)$$

where ρ_0 is a residual resistivity arising from both crystal and spin lattice disorder, BT^5 describes the resistivity resulting from electron-phonon scattering in the low-temperature limit and AT^2 accounts for electron-electron scattering. The fit yields the residual resistivity $\rho_0=13 \mu\Omega \text{ cm}$, the electron-electron and electron-phonon scattering coefficients $A=2.7(4) \cdot 10^{-9} \mu\Omega \text{ cm K}^{-2}$ and $B=3.0(1) \cdot 10^{-9} \mu\Omega \text{ cm K}^{-5}$, and the parameters of scattering by Einstein mode phonons: $\Theta_E^*=35(1)$ K and $\frac{KN}{M}=97(5) \mu\Omega \text{ cm K}$ (numbers in parentheses indicate

Table 1

Crystal structure parameters obtained from Rietveld fits to the XRD data collected at room temperature (ca. 20 °C). Numbers in parentheses indicate statistical uncertainties of the least significant digits. The site occupancies were not relaxed during the refinement. The *R*-factors presented in the table are corrected for background contribution.

ErV ₂ Al ₂₀	
Space group	<i>Fd</i> $\bar{3}m$ (no. 227)
<i>Z</i> (number of formula units per unit cell)	8
Pearson symbol	<i>cF</i> 184
Cell parameter (Å)	14.5175(2)
Cell volume (Å ³)	3059.68(13)
Molar weight (g·mol ⁻¹)	808.77
Density (g·cm ⁻³)	3.51
Atomic positions:	
Er (8a) <i>x</i> = <i>y</i> = <i>z</i> =	1/8
B _{iso} (Å ²)	2.34(3)
V (16d) <i>x</i> = <i>y</i> = <i>z</i> =	1/2
B _{iso} (Å ²)	1.27(4)
Al1 (16c) <i>x</i> = <i>y</i> = <i>z</i> =	0
B _{iso} (Å ²)	2.42(10)
Al2 (48f) <i>x</i> =	0.4871(1)
<i>y</i> = <i>z</i> =	1/8
B _{iso} (Å ²)	1.61(6)
Al3 (96g) <i>x</i> = <i>y</i> =	0.0596(1)
<i>z</i> =	0.3240(1)
B _{iso} (Å ²)	1.66(4)
Er–Er distance (Å)	6.2862(1)
Er–Al distances (Å): Al1	3.143
Al3	3.186(2)
Figures of merit:	
<i>R_p</i> (%)	11.7
<i>R_{wp}</i> (%)	11.6
<i>R_{exp}</i> (%)	10.8
χ^2 (%)	1.16

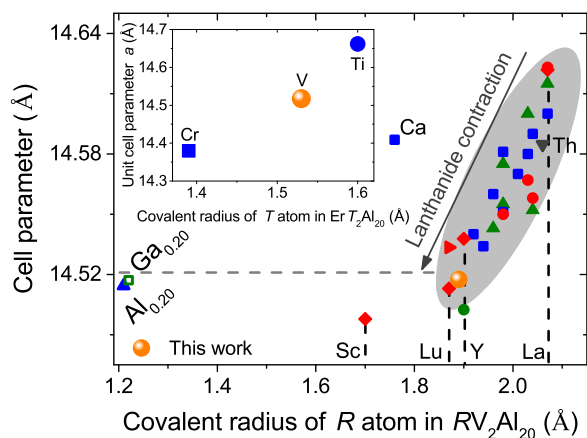


Fig. 4. The relation between unit cell parameter *a* and covalent radius of the cage-filling *R*(8a) atom for the reported *RV*₂Al₂₀ compounds. Unit cell parameter decreases with increasing atomic number from La to Lu due to the lanthanide contraction effect. For atoms smaller than Lu, cell parameters does not change significantly, as it is discussed in Ref. [17]. Inset shows unit cell parameters of *ErT*₂Al₂₀ (*T*=Ti, V, Cr). Covalent radii of the elements are given after Ref. [50], unit cell parameters: green triangles and blue squares – Ref. [45] and references therein, red circles – Ref. [30], red diamonds – Ref. [17], red triangle (YbV₂Al₂₀) – Ref. [44], blue triangle (VAl_{10.1}) – Ref. [15], green circle (TmV₂Al₂₀) – Ref. [43], green open square – Ref. [14], gray triangle (ThV₂Al₂₀) – Ref. [51], blue circle (ErTi₂Al₂₀) – [52]. (For interpretation of the references to color in this figure legend, the reader is referred to the web version of this article.)

the statistical uncertainties of the least significant digits).

The residual resistivity is of the same order of magnitude as reported for polycrystalline samples of YV₂Al₂₀, LaV₂Al₂₀ and

LuV₂Al₂₀, and almost 10 times lower than for ScV₂Al₂₀, where the presence of structural disorder was speculated [17], however, when comparing ρ_0 of magnetic and non-magnetic compounds it is important to take into account the effect of spin disorder in the former. Taking the ρ_0 value from the fit, a residual resistivity ratio $RRR = \rho(300\text{ K})/\rho_0 \approx 6.3$ is calculated, suggesting a relatively good sample quality.

3.3. Magnetic susceptibility

The temperature dependence of *dc* susceptibility $\chi(T)$ at 1 T field (Fig. 6(a)) is found to follow the Curie-Weiss law (Eq. 3):

$$\chi(T) = \frac{C}{T - \Theta_{CW}} + \chi_0 \quad (3)$$

where *C* is the Curie constant, Θ_{CW} is the Curie-Weiss temperature and χ_0 is the temperature-independent contribution to the susceptibility (coming both from the sample and a sample holder). Fig. 6(b) shows an inverse susceptibility vs. temperature plot emphasizing the Curie-Weiss character of magnetic susceptibility. The $\chi(T)$ data were fitted using the relationship given in Eq. (3). The Curie constant is related to the effective moment μ_{eff} associated with the magnetic ion as shown in Eq. (4):

$$C = \frac{N_A \mu_B^2 \mu_{\text{eff}}^2}{3k_B} \quad (4)$$

where *N_A* is the Avogadro number, μ_B – Bohr magneton, and *k_B* – Boltzmann constant. Values extracted from the fit are gathered in Table 2. The obtained effective magnetic moment (9.27 μ_B) is close to the value expected for a free Er³⁺ ion (9.5 μ_B) [54] and a small difference may be explained by both trace amounts of Al in the sample and effects of the crystal electric field. The close to zero yet negative value of Θ_{CW} suggests the presence of only very weak effective interactions between Er³⁺ magnetic moments. The field dependence of magnetization (see Fig. S2 of Supplementary material) shows a saturating character at low temperature (2 K), as expected for a Curie-Weiss paramagnet. Results of *ac* magnetic susceptibility at low constant field *H_{dc}*=5 Oe (*B_{dc}*=0.5 mT) show no sign of a magnetic transition down to 1.95 K (see Fig. 6(c)).

3.4. Specific heat

The specific heat of ErV₂Al₂₀ single crystal in the temperature range 1.95–30 K at zero magnetic field is shown in Fig. 7. Two anomalies are seen in the *C_p*/*T* vs. *T* plot: the first one below 5 K, attributed to the Schottky anomaly and second between 5 and 20 K, attributed to a low-energy Einstein phonon mode, observed in the isostructural ‘Einstein solid’ VAl_{10.1} [13,15].

The experimental data were fitted with a function including electronic, phonon and Schottky contributions:

$$C_p = C_{\text{electronic}} + C_{\text{Debye}} + C_{\text{Einstein}} + C_{\text{Schottky}}$$

$$C_{\text{electronic}} = \gamma T$$

$$C_{\text{Debye}} = \beta T^3$$

$$C_{\text{Einstein}} = A \cdot 3nR \left(\frac{\Theta_E}{T} \right)^2 \exp\left(\frac{\Theta_E}{T} \right) \left(\exp\left(\frac{\Theta_E}{T} \right) - 1 \right)^{-2}$$

$$C_{\text{Schottky}} = \frac{B}{T^2}$$

where γ is the Sommerfeld coefficient, β is a phonon specific heat parameter, Θ_E is a characteristic temperature of the low-energy Einstein mode, *n* is the number of atoms per formula unit, *R* is the gas constant, and *A*, *B* are fitting parameters. The Schottky contribution is described using a simplified, high-temperature limit formula.

The fit yields $\gamma = 118(3) \text{ mJ mol}^{-1} \text{ K}^{-2}$, $\beta = 0.882(9) \text{ mJ mol}^{-1} \text{ K}^{-4}$,

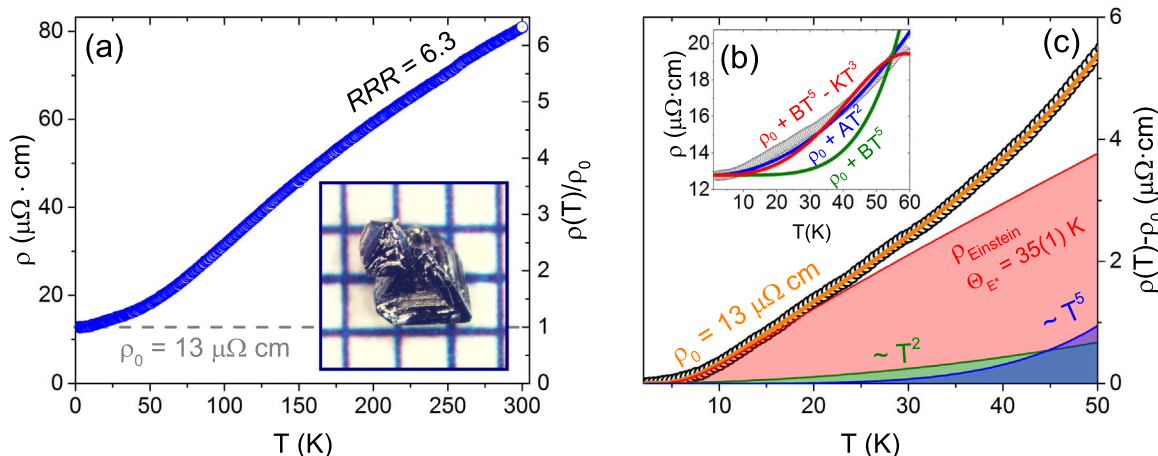


Fig. 5. (a): Temperature dependency of resistivity of $\text{ErV}_2\text{Al}_{20}$. Residual resistivity ratio $RRR=6.3$. Inset shows a sample aggregate of single crystals on a millimeter scale. (b): Low-temperature resistivity. Neither $\sim T^2$ dependence (blue line), $\sim T^5$ dependence (green line), nor $\sim T^5$ combined with Mott $\sim T^3$ term (red line) is sufficient to reproduce the experimental trend. (c): Fit (orange line) to the low-temperature resistivity (black circles) using Eq. (1), yielding residual resistivity $\rho_0=13 \mu\Omega \text{ cm}$ and the characteristic temperature of the Einstein mode $\Theta_E=35(1) \text{ K}$. Red line show a contribution of Einstein mode to the resistivity, green of electron-electron scattering and blue of electron-phonon scattering. (For interpretation of the references to color in this figure legend, the reader is referred to the web version of this article.)

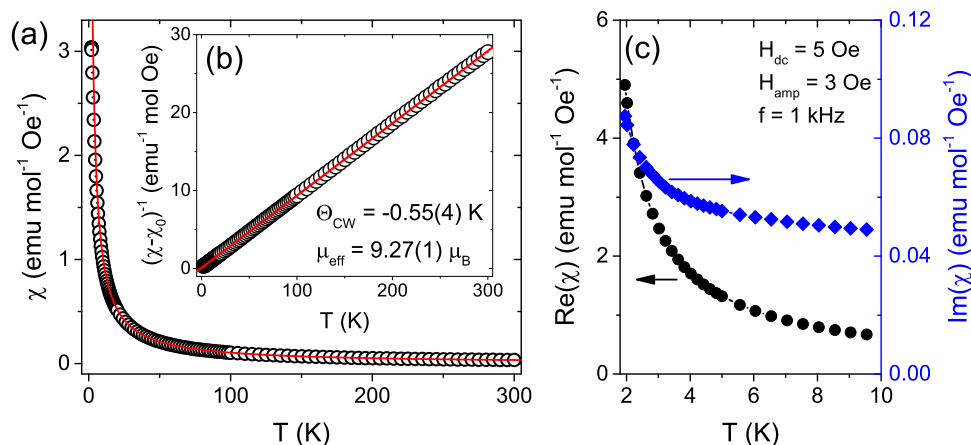


Fig. 6. (a) Magnetic susceptibility of $\text{ErV}_2\text{Al}_{20}$. The Curie-Weiss fit (Eq. 3) to the experimental points (black circles) is shown as a red solid line. (b) Inverse susceptibility (corrected for the temperature-independent contribution) shows a linear relation consistent with the Curie-Weiss law down to the lowest temperatures measured (1.95 K). (c) ac magnetic susceptibility at low dc field $H_{dc}=5 \text{ Oe}$. No magnetic transition is observed down to 1.95 K. The plot of magnetization vs. applied magnetic field at 2 K and 50 K is shown in Fig. S2 of the Supplementary material. (For interpretation of the references to color in this figure legend, the reader is referred to the web version of this article.)

Table 2

Results of Curie-Weiss fit to the dc susceptibility at 1 T. The temperature-independent susceptibility (χ_0) is not corrected for the contribution of sample holder.

C ($\text{emu K mol}^{-1} \text{ Oe}^{-1}$)	10.73 (2)
μ_{eff} (μ_B)	9.27(1)
Θ_{CW} (K)	-0.55(4)
χ_0 ($\text{emu mol}^{-1} \text{ Oe}^{-1}$)	$-1.4(1) \cdot 10^3$

$A=0.00294(4)$, $\Theta_E=43.7(3) \text{ K}$, $B=5.1(1) \text{ J K mol}^{-1}$. The individual contributions are plotted on Fig. 7. The large value of the γ coefficient compared to isostructural $\text{RV}_2\text{Al}_{20}$ ($R=\text{Sc, Y, La, Lu}$) compounds, for which it varies from 20 to $30 \text{ mJ mol}^{-1} \text{ K}^{-2}$ [17], may result from an insufficient modeling of the Schottky heat capacity contribution, however some enhancement of γ is possible due to the electron-phonon coupling. The Einstein temperature obtained from the specific heat fit (Θ_E) is higher than obtained from resistivity results (Θ_E^R) by ca. 20%. Such underestimation of the Einstein temperature in resistivity fits was reported previously for VA_{10+x} and $\text{Ga}_x\text{V}_2\text{Al}_{20}$ compounds [16].

In order to confirm the lattice origin of the anomaly attributed to an Einstein mode, specific heat measurements were performed in magnetic fields of 0.5–9 T (main panel of Fig. 8). The Schottky anomaly is shifted towards higher temperatures with an applied field due to

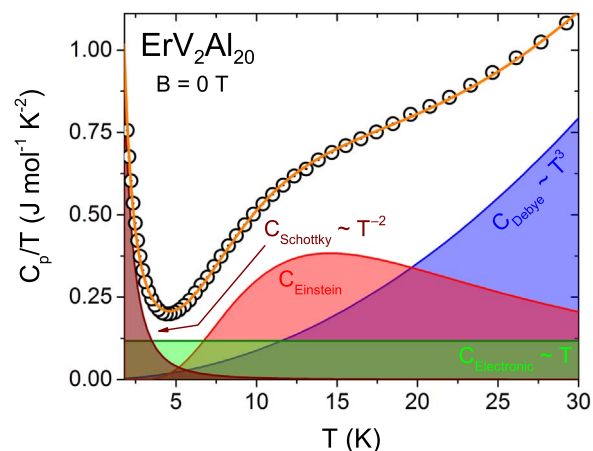


Fig. 7. Measured specific heat of $\text{ErV}_2\text{Al}_{20}$ at zero magnetic field (black circles). Orange line shows a fit to the experimental data including electronic, lattice, and Schottky components (see text). Contributions of individual components are plotted below: green – electronic, blue – Debye phonon heat capacity, red – low-energy Einstein phonon mode, brown – Schottky term. (For interpretation of the references to color in this figure legend, the reader is referred to the web version of this article.)

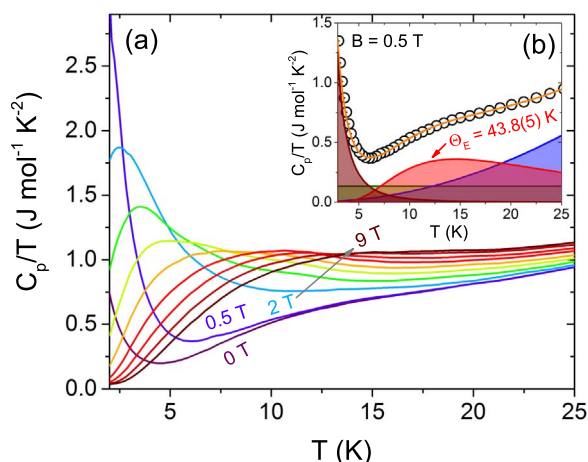


Fig. 8. (a) Specific heat of $\text{ErV}_2\text{Al}_{20}$ in magnetic fields $B=0.5\text{ T}$ and from 2 to 9 T with 1 T increments. The direction of magnetic field is parallel to the [111] crystallographic direction. Inset (b) shows a fit to the data measured at 0.5 T.

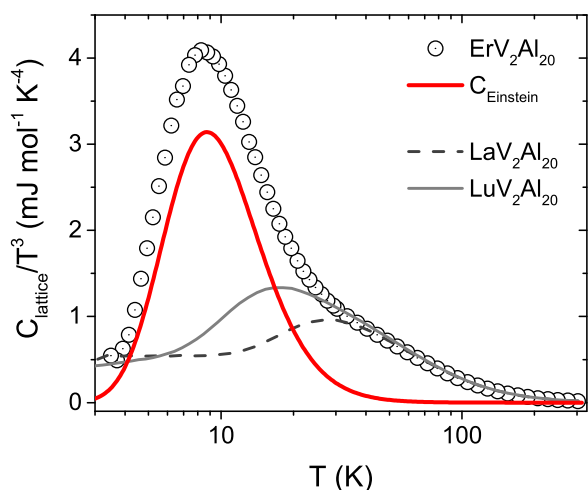


Fig. 9. Lattice specific heat of $\text{ErV}_2\text{Al}_{20}$ at zero magnetic field (black circles). Red line shows the contribution of a low-energy Einstein mode with $\Theta_E=43.7\text{ K}$. Lattice specific heat of $\text{LaV}_2\text{Al}_{20}$ (gray dashed line) and $\text{LuV}_2\text{Al}_{20}$ (gray solid line) are plotted for comparison after Ref. [17]. (For interpretation of the references to color in this figure legend, the reader is referred to the web version of this article.)

Zeeman splitting of the Er^{3+} energy levels, while the anomaly attributed to the Einstein mode is not affected. Fig. 8(b) shows a fit to the specific heat at 0.5 T yielding the same Einstein temperature as obtained from the fit in zero field $\Theta_E=43.8(5)\text{ K}$. At higher magnetic fields the Einstein contribution to specific heat is already obscured by the large Schottky anomaly.

In a simple Debye model the β coefficient is related to the Debye temperature Θ_D :

$$\Theta_D = \sqrt{\frac{12\pi^4 nR}{5\beta}} \quad (6)$$

The estimated value of $\Theta_D = 370(1)\text{ K}$ is comparable to the value reported recently for $\text{UNb}_2\text{Al}_{20}$ (381 K) [55], but significantly lower than obtained for $\text{RV}_2\text{Al}_{20}$ ($R=\text{Sc}, \text{Y}, \text{La}, \text{Lu}$) for which the Debye temperature is in the order of 500 K, and for $\text{UCr}_2\text{Al}_{20}$ (474 K) and $\text{ThCr}_2\text{Al}_{20}$ (457 K) [56]. This difference may be explained by both the effect of low-energy modes and systematic error in estimation of β parameter caused eg. by applying the low-temperature $\sim T^{-3}$ expansion of the Debye specific heat in too wide temperature range.

The fitted parameters B and γ were used to obtain a lattice specific heat (C_{lattice}) by subtracting the specific heat of the Schottky and electronic term from the experimental data. The results are shown in

Fig. 9. The peak at approx. 8.5 K confirms the presence of an Einstein mode with $\Theta_E \approx 5.8.5 \approx 43\text{ K}$. The peak observed in $\text{ErV}_2\text{Al}_{20}$ is also seen in the specific heat of $\text{LaV}_2\text{Al}_{20}$ and $\text{LuV}_2\text{Al}_{20}$, however the characteristic temperature is significantly higher (ca. 140 and 90 K, respectively). A low-temperature Einstein mode was also observed in an isostructural $\text{VAl}_{10,1}$ compound with $\Theta_E=21\text{ K}$ [13], approx. twice lower than for $\text{ErV}_2\text{Al}_{20}$. Since the mode in $\text{VAl}_{10,1}$ was attributed to localized anharmonic ‘rattling’ of Al atoms occupying the 8a sites inside Al atom cages, the low-energy Einstein mode in $\text{ErV}_2\text{Al}_{20}$ arises likely from a ‘rattling’ of the cage-filling Er atoms. Relatively large thermal displacement parameters obtained from the Rietveld fit suggests that the mode could be associated with vibrations of Er(8a) or Al1(16c) atoms, both positioned inside large cages (see Fig. 1(b,d)). In order to clarify this, phonon structure calculations or inelastic neutron scattering experiments should be performed.

4. Conclusions

Single crystals of the previously unreported $\text{ErV}_2\text{Al}_{20}$ compound crystallizing with the $\text{CeCr}_2\text{Al}_{20}$ -type structure were successfully grown using the flux-growth technique. The crystal structure of the new compound was studied by means of powder X-ray diffraction and Rietveld refinement.

Magnetization measurements show Curie-Weiss paramagnetic character with an effective magnetic moment $\mu_{\text{eff}}=9.27(1)\mu_B$ close to the expected value for trivalent Er^{+3} ion. The Curie-Weiss temperature $\Theta_{\text{CW}}=-0.55(4)\text{ K}$ is close to zero suggesting very weak effective interactions between Er^{3+} magnetic moments.

Specific heat measurements show a presence of two anomalies at low temperatures: while one, sharper, is attributed to the Schottky anomaly, the second, broader, is found to arise from the presence of a low-energy Einstein mode ($\Theta_E=44\text{ K}$), probably associated with the large amplitude vibrations of either Er(8a) or Al1(16c) atoms positioned in oversized cages. Therefore, $\text{ErV}_2\text{Al}_{20}$ is a new aluminide cage compound in which the ‘rattling’ effect is observed. Further studies, including phonon structure calculations and inelastic neutron scattering experiments, will be necessary to shed light on the origin of the low-energy Einstein mode. An interesting question to study is also how the ‘rattling’ of paramagnetic lanthanide atom affects the magnetic properties of the material.

Acknowledgments

The project was supported by the National Science Center (Poland) Grant (DEC-2012/07/E/ST3/00584).

Appendix A. Supporting information

Supplementary data associated with this article can be found in the online version at doi:10.1016/j.jssc.2016.09.029.

References

- [1] J. Teyssier, R. Lortz, A. Petrovic, D. van der Marel, V. Filippov, N. Shitsevalova, Effect of electron-phonon coupling on the superconducting transition temperature in dodecaboride superconductors: a comparison of LuB_{12} with ZrB_{12} , Phys. Rev. B 78 (2008) 134504. <http://dx.doi.org/10.1103/PhysRevB.78.134504>.
- [2] R. Lortz, R. Viennois, A. Petrovic, Y. Wang, P. Toulemonde, C. Meingast, M.M. Kozá, H. Mutka, A. Bossak, A.S. Miguel, Phonon density of states, anharmonicity, electron-phonon coupling, and possible multigap superconductivity in the clathrate superconductors $\text{Ba}_8\text{Si}_{46}$ and $\text{Ba}_{24}\text{Si}_{106}$: factors behind large difference in T_c , Phys. Rev. B 77 (2008) 224507. <http://dx.doi.org/10.1103/PhysRevB.77.224507>.
- [3] J. Fulmer, O.I. Lebedev, V.V. Roddatis, D.C. Kaseman, S. Sen, J.-A. Dolyniuk, K. Lee, A.V. Olenov, K. Kovnir, Clathrate $\text{Ba}_8\text{Au}_{16}\text{P}_{30}$: the ‘gold standard’ for lattice thermal conductivity, J. Am. Chem. Soc. 135 (2013) 12313–12323. <http://dx.doi.org/10.1021/ja4052679>.
- [4] M. Beekman, W. Schnelle, H. Borrmann, M. Baitinger, Y. Grin, G.S. Nolas, Intrinsic electrical and thermal properties from single crystals of $\text{Na}_{24}\text{Si}_{136}$, Phys. Rev. Lett.

- 104 (2010) 18301. <http://dx.doi.org/10.1103/PhysRevLett.104.018301>.
- [5] B.C. Sales, D. Mandrus, B.C. Chakoumakos, V. Keppens, J.R. Thompson, Filled skutterudite antimonides: electron crystals and phonon glasses, *Phys. Rev. B* 56 (1997) 15081–15089. <http://dx.doi.org/10.1103/PhysRevB.56.15081>.
- [6] B.C. Sales, B.C. Chakoumakos, D. Mandrus, Thermoelectric properties of thallium-filled skutterudites, *Phys. Rev. B* 61 (2000) 2475–2481. <http://dx.doi.org/10.1103/PhysRevB.61.2475>.
- [7] H. Luo, J.W. Krizan, L. Muechler, N. Haldolarachchige, T. Klimczuk, W. Xie, M.K. Fuccillo, C. Felser, R.J. Cava, A large family of filled skutterudites stabilized by electron count, *Nat. Commun.* 6 (2015). <http://dx.doi.org/10.1038/ncomms7489>.
- [8] Y. Nagao, J. Yamaura, H. Ogusu, Y. Okamoto, Z. Hiroi, Rattling-induced superconductivity in the β -pyrochlore oxides AO_2O_6 , *J. Phys. Soc. Jpn.* 78 (2009) 64702. <http://dx.doi.org/10.1143/JPSJ.78.064702>.
- [9] M.M. Koza, A. Leithe-Jasper, E. Sischka, W. Schnelle, H. Borrmann, H. Mutka, Y. Grin, Effect of the electropositive elements A=Sc, La, and Ce on the microscopic dynamics of $\text{AV}_2\text{Al}_{20}$, *Phys. Chem. Chem. Phys.* 16 (2014) 27119–27133. <http://dx.doi.org/10.1039/C4CP04097J>.
- [10] J. Teyssier, A. Kuzmenko, D. van der Marel, R. Lortz, A. Junod, V. Filipov, N. Shitsevalova, Electronic and optical properties of ZrB_{12} and YB_6 . Discussion on electron-phonon coupling, *Phys. Status Solidi C* 3 (2006) 3114–3117. <http://dx.doi.org/10.1002/pssc.200567023>.
- [11] R. Lortz, Y. Wang, U. Tutsch, S. Abe, C. Meingast, P. Popovich, W. Knafo, N. Shitsevalova, Y.B. Paderno, A. Junod, Superconductivity mediated by a soft phonon mode: specific heat, resistivity, thermal expansion, and magnetization of YB_6 , *Phys. Rev. B* 73 (2006) 24512. <http://dx.doi.org/10.1103/PhysRevB.73.024512>.
- [12] Z. Hiroi, J. Yamaura, K. Hattori, Rattling good superconductor: β -pyrochlore oxides AO_2O_6 , *J. Phys. Soc. Jpn.* 81 (2011) 11012. <http://dx.doi.org/10.1143/JPSJ.81.011012>.
- [13] D.J. Safarik, T. Klimczuk, A. Llobet, D.D. Byler, J.C. Lashley, J.R. O'Brien, N.R. Dilley, Localized anharmonic rattling of Al atoms in $\text{VAL}_{10,1}$, *Phys. Rev. B* 85 (2012) 14103. <http://dx.doi.org/10.1103/PhysRevB.85.014103>.
- [14] A. Onosaka, Y. Okamoto, J. Yamaura, Z. Hiroi, Superconductivity in the Einstein solid $\text{A}_x\text{V}_2\text{Al}_{20}$ (A=Al and Ga), *J. Phys. Soc. Jpn.* 81 (2012) 23703. <http://dx.doi.org/10.1143/JPSJ.81.023703>.
- [15] T. Klimczuk, M. Szwalska, D. Kaczorowski, J.R. O'Brien, D.J. Safarik, Superconductivity in the Einstein solid $\text{VAL}_{10,1}$, *J. Phys.: Condens. Matter* 24 (2012) 365701. <http://dx.doi.org/10.1088/0953-8984/24/36/365701>.
- [16] Z. Hiroi, A. Onosaka, Y. Okamoto, J. Yamaura, H. Harima, Rattling and superconducting properties of the cage compound $\text{Ga}_x\text{V}_2\text{Al}_{20}$, *J. Phys. Soc. Jpn.* 81 (2012) 124707. <http://dx.doi.org/10.1143/JPSJ.81.124707>.
- [17] M.J. Winiarski, B. Wiendlocha, M. Sternik, P. Wiśniewski, J.R. O'Brien, D. Kaczorowski, T. Klimczuk, Rattling-enhanced superconductivity in $\text{MV}_2\text{Al}_{20}$ (M=Sc, Lu, Y) intermetallic cage compounds, *Phys. Rev. B* 93 (2016) 134507. <http://dx.doi.org/10.1103/PhysRevB.93.134507>.
- [18] F.C. Frank, J.S. Kasper, Complex alloy structures regarded as sphere packings. I. Definitions and basic principles, *Acta Crystallogr.* 11 (1958) 184–190. <http://dx.doi.org/10.1107/S0365110X58000487>.
- [19] H. Nyman, S. Andersson, B.G. Hyde, M. O'Keeffe, The pyrochlore structure and its relatives, *J. Solid State Chem.* 26 (1978) 123–131.
- [20] K. Momma, F. Izumi, VESTA 3 for three-dimensional visualization of crystal, volumetric and morphology data, *J. Appl. Crystallogr.* 44 (2011) 1272–1276. <http://dx.doi.org/10.1107/S0021889811038970>.
- [21] A. Leithe-Jasper, A. Sato, T. Tanaka, Refinement of the crystal structure of zirconium dodecaboride, ZrB_{12} , at 140 K and 293 K., *Zeitschrift für Kristallographie: New Crystal Structures* 217 (2002) 319–320. <http://dx.doi.org/10.1524/nrcs.2002.217.1.319>.
- [22] S. Grazulis, D. Chateigner, R.T. Downs, A.F.T. Yokochi, M. Quiros, L. Lutterotti, E. Manakova, J. Butkus, P. Moeck, A. Le Bail, Crystallography open database - an open-access collection of crystal structures, *J. Appl. Crystallogr.* 42 (2009) 726–729. <http://dx.doi.org/10.1107/S0021889809016690>.
- [23] D.J. Braun, W. Jeitschko, Preparation and structural investigations of antimonides with the $\text{LaFe}_4\text{P}_{12}$ structure, *J. Less Common Met.* 72 (1980) 147–156. [http://dx.doi.org/10.1016/0022-5088\(80\)90260-X](http://dx.doi.org/10.1016/0022-5088(80)90260-X).
- [24] Y. Xu, M. Yamazaki, P. Villars, Inorganic materials database for exploring the nature of material, *Jpn. J. Appl. Phys.* 50 (2011) 11RH02. <http://dx.doi.org/10.1143/JJAP.50.11RH02>.
- [25] S. Yamanaka, E. Enishi, H. Fukuoka, M. Yasukawa, High-pressure synthesis of a new silicon clathrate superconductor, $\text{Ba}_8\text{Si}_{46}$, *Inorg. Chem.* 39 (2000) 56–58. <http://dx.doi.org/10.1021/ic990778p>.
- [26] J.-I. Yamaura, S. Yonezawa, Y. Muraoka, Z. Hiroi, Crystal structure of the pyrochlore oxide superconductor KOs_2O_6 , *J. Solid State Chem.* 179 (2006) 336–340. <http://dx.doi.org/10.1016/j.jssc.2005.10.039>.
- [27] A. Onosaka, Y. Okamoto, J. Yamaura, T. Hirose, Z. Hiroi, Large diamagnetism of $\text{AV}_2\text{Al}_{20}$ (A=Y and La), *J. Phys. Soc. Jpn.* 81 (2012) 123702. <http://dx.doi.org/10.1143/JPSJ.81.123702>.
- [28] T. Hirose, Y. Okamoto, J. Yamaura, Z. Hiroi, Large diamagnetic susceptibility from petit fermi surfaces in $\text{LaV}_2\text{Al}_{20}$, *J. Phys. Soc. Jpn.* 84 (2015) 113701. <http://dx.doi.org/10.7566/JPSJ.84.113701>.
- [29] O. Moze, L.D. Tung, J.J.M. Franse, K.H.J. Buschow, Crystal structure and magnetic properties of $\text{CeV}_2\text{Al}_{20}$ and $\text{CeCr}_2\text{Al}_{20}$, *J. Alloy. Compd.* 268 (1998) 39–41. [http://dx.doi.org/10.1016/S0925-8388\(97\)00586-0](http://dx.doi.org/10.1016/S0925-8388(97)00586-0).
- [30] M.J. Kangas, D.C. Schmitt, A. Sakai, S. Nakatsuji, J.Y. Chan, Structure and physical properties of single crystal $\text{PrCr}_2\text{Al}_{20}$ and $\text{CeM}_2\text{Al}_{20}$ (M=V, Cr): a comparison of compounds adopting the $\text{CeCr}_2\text{Al}_{20}$ structure type, *J. Solid State Chem.* 196 (2012) 274–281. <http://dx.doi.org/10.1016/j.jssc.2012.06.035>.
- [31] M. Tsujimoto, Y. Matsumoto, T. Tomita, A. Sakai, S. Nakatsuji, Heavy-fermion superconductivity in the quadrupole ordered state of $\text{PrV}_2\text{Al}_{20}$, *Phys. Rev. Lett.* 113 (2014) 267001. <http://dx.doi.org/10.1103/PhysRevLett.113.267001>.
- [32] K. Araki, Y. Shimura, N. Kase, T. Sakakibara, A. Sakai, S. Nakatsuji, Magnetization and specific heat of the cage compound $\text{PrV}_2\text{Al}_{20}$, *JPS Conf. Proc.* 3 (2014) 011093. <http://dx.doi.org/10.7566/JPSCP.3.011093>.
- [33] T.J. Sato, S. Iwaka, Y. Nambu, T. Yamazaki, T. Hong, A. Sakai, S. Nakatsuji, Ferroquadrupolar ordering in $\text{PrTi}_2\text{Al}_{20}$, *Phys. Rev. B* 86 (2012) 184419. <http://dx.doi.org/10.1103/PhysRevB.86.184419>.
- [34] A. Sakai, K. Kuga, S. Nakatsuji, Superconductivity in the ferroquadrupolar state in the quadrupolar Kondo lattice $\text{PrTi}_2\text{Al}_{20}$, *J. Phys. Soc. Jpn.* 81 (2012) 83702. <http://dx.doi.org/10.1143/JPSJ.81.083702>.
- [35] T. Namiki, Y. Murata, K. Baba, K. Shimojo, K. Nishimura, Magnetic and electronic properties of $\text{NdTi}_2\text{Al}_{20}$ (T=Ti, V, Cr), *JPS Conf. Proc.* 3 (2014) 011055. <http://dx.doi.org/10.7566/JPSCP.3.011055>.
- [36] A. Sakai, S. Nakatsuji, Strong valence fluctuation effects in $\text{SmTr}_2\text{Al}_{20}$ (Tr=Ti, V, Cr), *Phys. Rev. B* 84 (2011) 201106. <http://dx.doi.org/10.1103/PhysRevB.84.201106>.
- [37] A. Yamada, R. Higashinaka, R. Miyazaki, K. Fushiya, T.D. Matsuda, Y. Aoki, W. Fujita, H. Harima, H. Sato, Anomalous field-insensitive correlated electron behaviors in $\text{SmT}_2\text{Al}_{20}$, *J. Phys. Soc. Jpn.* 82 (2013) 123710. <http://dx.doi.org/10.7566/JPSJ.82.123710>.
- [38] J. Chi, Y. Li, W. Gou, V. Goruganti, K.D.D. Rathnayaka, J.H. Ross Jr., Kondo lattice behavior and magnetic field effects in $\text{Al}_2\text{O}_3\text{V}_2\text{Eu}$, *Physica B: Condens. Matter* 403 (2008) 1426–1427. <http://dx.doi.org/10.1016/j.physb.2007.10.308>.
- [39] P. Swatek, D. Kaczorowski, Magnetic properties of $\text{EuCr}_2\text{Al}_{20}$, *J. Magn. Magn. Mater.* 416 (2016) 348–352. <http://dx.doi.org/10.1016/j.jmmm.2016.04.086>.
- [40] R.K. Kumar, H.S. Nair, R. Christian, A. Thamizavel, A.M. Strydom, Magnetic, specific heat and electrical transport properties of Frank–Kasper cage compounds $\text{RTM}_2\text{Al}_{20}$ [R=Eu, Gd and La; TM=V, Ti], *J. Phys.: Condens. Matter* 28 (2016) 436002. <http://dx.doi.org/10.1088/0953-8984/28/43/436002>.
- [41] Y. Verbovitsky, K. Latka, K. Tomala, The crystal structure and magnetic properties of the $\text{GdV}_2\text{Al}_{20}$ and $\text{GdCr}_2\text{Al}_{20}$ ternary compounds, *J. Alloy. Compd.* 442 (2007) 334–336. <http://dx.doi.org/10.1016/j.jallcom.2006.07.148>.
- [42] N. Kase, Y. Shimura, S. Kittaka, T. Sakakibara, S. Nakatsuji, T. Nakano, N. Takeda, J. Akimitsu, Antiferromagnetic transition of the caged compound $\text{TmTi}_2\text{Al}_{20}$, *J. Phys.: Conf. Ser.* 592 (2015) 12052. <http://dx.doi.org/10.1088/1742-6596/592/1/012052>.
- [43] Q. Lei, T. Namiki, Y. Isikawa, K. Nishimura, W.D. Hutchison, Magnetic and thermal properties of $\text{TmV}_2\text{Al}_{20}$ single crystals, *J. Phys. Soc. Jpn.* 85 (2016) 34709. <http://dx.doi.org/10.7566/JPSJ.85.034709>.
- [44] R. Higashinaka, A. Nakama, M. Ando, M. Watanabe, Y. Aoki, H. Sato, Magnetic and transport properties of $\text{YbTi}_2\text{Al}_{20}$, *J. Phys.: Conf. Ser.* 273 (2011) 12033. <http://dx.doi.org/10.1088/1742-6596/273/1/012033>.
- [45] V.M.T. Thiede, W. Jeitschko, S. Niemann, T. Ebel, $\text{EuTa}_2\text{Al}_{20}$, $\text{Ca}_6\text{W}_4\text{Al}_{43}$ and other compounds with $\text{CeCr}_2\text{Al}_{20}$ and $\text{Ho}_2\text{Mo}_4\text{Al}_{43}$ type structures and some magnetic properties of these compounds, *J. Alloy. Compd.* 267 (1998) 23–31. [http://dx.doi.org/10.1016/S0925-8388\(97\)00532-X](http://dx.doi.org/10.1016/S0925-8388(97)00532-X).
- [46] P.C. Canfield, Z. Fisk, Growth of single crystals from metallic fluxes, *Philos. Mag. Part B* 65 (1992) 1117–1123. <http://dx.doi.org/10.1080/13642819208215073>.
- [47] P.C. Canfield, T. Kong, U.S. Kaluarachchi, N.H. Jo, Use of frit-disc crucibles for routine and exploratory growth of single crystalline samples, *Philos. Mag.* 96 (2016) 84–92. <http://dx.doi.org/10.1080/14786435.2015.1122248>.
- [48] J. Rodríguez-Carvajal, Recent advances in magnetic structure determination by neutron powder diffraction, *Physica B: Condens. Matter* 192 (1993) 55–69. [http://dx.doi.org/10.1016/092-14526\(93\)90108-1](http://dx.doi.org/10.1016/092-14526(93)90108-1).
- [49] H.M. Rietveld, A profile refinement method for nuclear and magnetic structures, *J. Appl. Crystallogr.* 2 (1969) 65–71. <http://dx.doi.org/10.1107/S0021889869006558>.
- [50] B. Cordero, V. Gómez, A.E. Platero-Prats, M. Revés, J. Echeverría, E. Cremades, F. Barragán, S. Alvarez, Covalent radii revisited, *Dalton Trans.* (2008) 2832–2838. <http://dx.doi.org/10.1039/B801115J>.
- [51] A.I. Bram, A. Venkert, L. Meshi, Characterization of new aluminides found in the $\text{ThT}_2\text{Al}_{20}$ alloys (where T=Ti, V, Mn), *J. Alloy. Compd.* 641 (2015) 1–6. <http://dx.doi.org/10.1016/j.jallcom.2015.03.247>.
- [52] S. Niemann, W. Jeitschko, Ternary aluminides $\text{AT}_2\text{Al}_{20}$ (A=rare earth elements and uranium; T=Ti, Nb, Ta, Mo, and W) with $\text{CeCr}_2\text{Al}_{20}$ -Type Structure, *J. Solid State Chem.* 114 (1995) 337–341. <http://dx.doi.org/10.1006/jssc.1995.1052>.
- [53] J.R. Cooper, Electrical resistivity of an Einstein solid, *Phys. Rev. B* 9 (1974) 2778–2780. <http://dx.doi.org/10.1103/PhysRevB.9.2778>.
- [54] Charles Kittel, *Introduction to Solid State Physics*, 8th ed., Wiley, Hoboken, 2004.
- [55] C. Moussa, A. Berche, M. Pasturel, J. Barbosa, B. Stepnik, S. Dubois, O. Tougaard, The U-Nb-Al ternary system: experimental and simulated investigations of the phase equilibria and study of the crystal structure and electronic properties of the intermediate phases, *J. Alloy. Compd.* 691 (2017) 893–905. <http://dx.doi.org/10.1016/j.jallcom.2016.08.257>.
- [56] P. Swatek, D. Kaczorowski, Magnetic and electrical properties of $\text{UCr}_2\text{Al}_{20}$ single crystals, *J. Solid State Chem.* 191 (2012) 191–194. <http://dx.doi.org/10.1016/j.jssc.2012.03.018>.